JACS
JOURNAL OF THE AMERICAN CHEMICAL SOCIETY
Article
pubs.acs.org/JACS

Characterization of [4Fe-4S] Cluster Vibrations and Structure in Nitrogenase Fe Protein at Three Oxidation Levels via Combined NRVS, EXAFS, and DFT Analyses

Devrani Mitra,[†,#] Simon J. George,[‡,§,#] Yisong Guo,[⊥] Saeed Kamali,[‡] Stephen Keable,[∥] John W. Peters,[∥] Vladimir Pelmenschikov,*[,∞] David A. Case,[¶] and Stephen P. Cramer*[,‡,§]

[†]Department of Biochemistry and Molecular Biology, The University of Chicago, Chicago, Illinois 60637, United States
[‡]Department of Chemistry, University of California at Davis, Davis, California 95616, United States
[§]Advanced Biological and Environmental X-ray Spectroscopy Facility, Physical Biosciences Division, Lawrence Berkeley National Laboratory, Berkeley, California 94720, United States
[⊥]Department of Applied Science, University of California at Davis, Davis, California 95616, United States
[∥]Department of Chemistry, Montana State University, Bozeman, Montana 59717, United States
[∞]Institut für Chemie, Technische Universität Berlin, 10623 Berlin, Germany
[¶]Department of Chemistry and Chemical Biology and BioMaPS Institute, Rutgers University, Piscataway, New Jersey 08854, United States

Supporting Information

ABSTRACT: *Azotobacter vinelandii* nitrogenase Fe protein (*Av*2) provides a rare opportunity to investigate a [4Fe-4S] cluster at three oxidation levels in the same protein environment. Here, we report the structural and vibrational changes of this cluster upon reduction using a combination of NRVS and EXAFS spectroscopies and DFT calculations. Key to this work is the synergy between these three techniques as each generates highly complementary information and their analytical methodologies are interdependent. Importantly, the spectroscopic samples contained no glassing agents. NRVS and DFT reveal a systematic 10−30 cm^{-1} decrease in Fe−S stretching frequencies with each added electron. The "oxidized" $[4Fe\text{-}4S]^{2+}$ state spectrum is consistent with and extends previous resonance Raman spectra. For the "reduced" $[4Fe\text{-}4S]^{1+}$ state in Fe protein, and for any "all-ferrous" $[4Fe\text{-}4S]^{0}$ cluster, these NRVS spectra are the first available vibrational data. NRVS simulations also allow estimation of the vibrational disorder for Fe−S and Fe−Fe distances, constraining the EXAFS analysis and allowing structural disorder to be estimated. For oxidized *Av*2, EXAFS and DFT indicate nearly equal Fe−Fe distances, while addition of one electron decreases the cluster symmetry. However, addition of the second electron to form the all-ferrous state induces significant structural change. EXAFS data recorded to k = 21 $Å^{-1}$ indicates a 1:1 ratio of Fe−Fe interactions at 2.56 Å and 2.75 Å, a result consistent with DFT. Broken symmetry (BS) DFT rationalizes the interplay between redox state and the Fe−S and Fe−Fe distances as predominantly spin-dependent behavior inherent to the [4Fe-4S] cluster and perturbed by the *Av*2 protein environment.

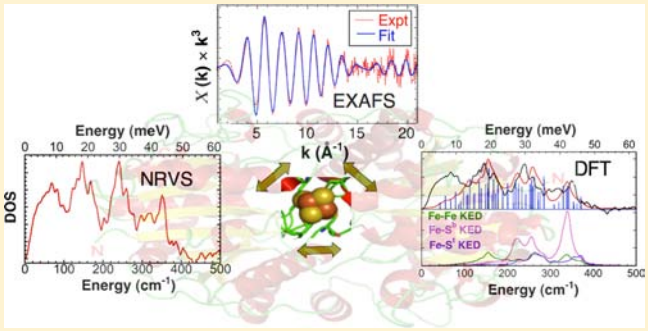

INTRODUCTION

The biological fixation of dinitrogen to ammonia is most commonly achieved by the MoFe nitrogenase (N_2ase) enzyme systems.[1] These bacterial enzymes comprise two component proteins: the MoFe protein that contains FeMo cofactor active site, and the Fe protein that contains a single [4Fe-4S] cubane iron−sulfur cluster. While the MoFe protein contains the site of N_2 binding and subsequent reduction, the Fe protein functions as a highly specific electron donor for the MoFe protein. During a catalytic cycle the Fe protein associates and dissociates from the MoFe protein several times, each time delivering electrons from its [4Fe-4S] cluster to the MoFe protein in a reaction that is dependent on the hydrolysis of MgATP.[1]

The Fe protein has drawn enormous interest. X-ray diffraction (XRD) studies have provided several crystal structures,[2,3] and these all show that the Fe protein is a dimer whose identical 32 kDa subunits symmetrically coordinate the [4Fe-4S] cluster with four cysteinyl ligands, two from each subunit (Cys 97 and Cys 132 in the *Av* sequence) (Figure 1). Spectroscopic studies have been

Received: July 18, 2012
Published: January 1, 2013

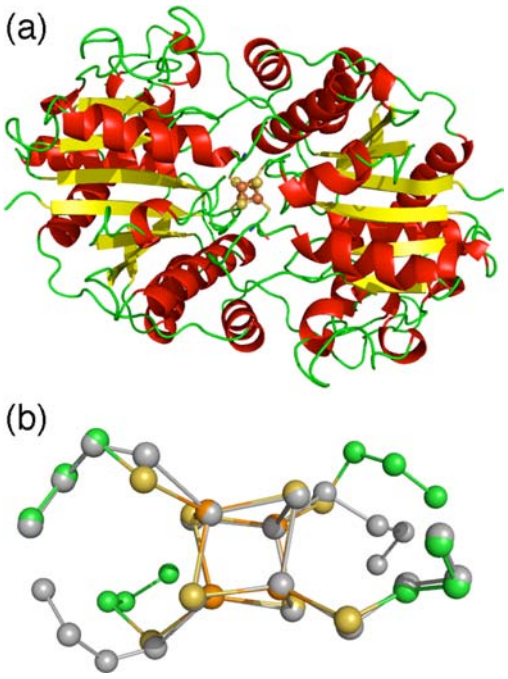

Figure 1. (a) Overall structure of *Av2* (PDB 2NIP[2]). (b) close-up view of [4Fe-4S] site in *Av2* (color) compared to a hypothetical [4Fe-4S](SCCC)$_4$ model with D_{2d} core symmetry and C_2 overall symmetry (gray).

performed using a range of techniques including: electron paramagnetic resonance (EPR),[4] Mössbauer,[4] small-angle X-ray scattering (SAXS),[5] resonance Raman,[6,7] circular dichroism (CD),[8] and extended X-ray absorption fine structure (EXAFS)[8−11] spectroscopies. This interest has arisen for many reasons. First, there is the Fe protein's ability to couple ATP hydrolysis with electron transfer.[1] Second, it plays a significant biosynthetic role in the maturation of its MoFe partner.[12] Third, its [4Fe-4S] cluster can be reduced to the [4Fe-4S]^0 redox level where all the Fe are in the ferrous Fe^{2+} oxidation state,[11,13] in addition to the more usual "oxidized" [4Fe-4S]$^{2+}$ and the "reduced" [4Fe-4S]$^{1+}$ forms. It has been suggested that this "all-ferrous" state may have a physiological role in that the electron transfer between the Fe and MoFe proteins might be a two-electron process employing the [4Fe-4S]$^{0/2+}$ redox couple, a proposal consistent with the observed physiological range of the $P^{0/2+}$ $2e^-$ redox couple of the P-cluster electron receptor in the MoFe protein. However, the latest findings propose that each of the nitrogenase metal cofactors cycles through only two redox states during catalysis,[14] implying "classic" [4Fe-4S]$^{1+/2+}$ redox behavior for the cluster in *Av2*. Nevertheless, interest in the all-ferrous form over the past decade has inspired synthesis of the [4Fe-4S]^0 complexes[15,16] and several theoretical studies.[17−19] A fourth notable property of the Fe protein is that the biophysical properties of the [4Fe-4S] cluster are dependent on both whether nucleotides are bound and agents like glycerol are present. The addition of 50% glycerol, for instance, converts the spin-state of the reduced state from predominately $S = 3/2$ to predominately $S = 1/2$.[20] Similarly, addition of MgATP changes the protein conformation about the cluster,[7] with concomitant changes to its EPR and other spectroscopic properties.[9] Finally it is important to note that some of these special characteristics of the Fe protein may have analogues in other proteins, where ATP hydrolysis-dependent electron transfer[21] and [4Fe-4S]^0 redox levels[22] have been observed.

The rare opportunity to investigate the same Fe−S cluster in three different redox states and to understand the concomitant electron transfer behavior makes the Fe protein particularly interesting. A detailed understanding of the changes in the vibrational structure of the [4Fe-4S] center with redox state would undoubtedly be valuable, but unfortunately only the oxidized level has proven accessible to resonance Raman spectroscopy.[6,7] Similarly, the changes in cluster conformation with oxidation state are also relevant to electron transfer, but again data are limited. The available crystal structures are most likely restricted to the two reduced states. For the Fe protein from *Azotobacter vinelandii* (*Av*), *Av2*, structures 2NIP[2] and 1G5P[3] are different refinements of the same 2.2 Å resolution set with the cluster oxidation state unclear but probably at the dithionite-reduced [4Fe-4S]$^{1+}$ level. For the *Clostridium pasteurianum* Fe protein, *Cp2*, structure 1CP2 has been measured with a resolution of 1.93 Å,[2] again most likely with a [4Fe-4S]$^{1+}$ cluster. The all-ferrous [4Fe-4S]^0 state of *Av2* has also been reported in structure 1G1M at 2.25 Å.[3] One interesting observation is that, when compared to all structurally characterized Fe−S cluster-containing proteins, the Fe protein has the largest solvent-accessible surface area around its cluster.[2] This is readily apparent in Figure 1a and might well account for its ability to attain three distinct oxidation states as well as its sensitivity to reagents such as glycerol. Finally, the structural technique EXAFS has also been used to probe the detailed structure of the [4Fe-4S] cubane.[8−11] While the spectra from the oxidized and reduced states are typically interpreted using relatively symmetric models, Musgrave and co-workers[11] interpreted the spectrum of the all-ferrous state in terms of a significant conformational deformation of the cluster with two shorter and one longer Fe−Fe distances at 2.53 Å and 2.77 Å. More recently, Blank et al. have suggested a similar distortion for the reduced state.[10] However, the samples for EXAFS studies almost always include at least 10−20% glycerol or similar glassing agent, which is known to affect Fe protein properties. Clearly, a systematic EXAFS study of the Fe protein using samples without glassing agent would have considerable interest.

In this contribution we use the novel technique of ^{57}Fe nuclear resonance vibrational spectroscopy (NRVS), together with Fe K-edge EXAFS spectroscopy and density functional theory (DFT) analyses to probe and rationalize the changes in structure and vibrational dynamics of the [4Fe-4S] cluster in the three experimentally accessible oxidation levels of the Fe protein from *A. vinelandii*, *Av2*. NRVS and EXAFS have been shown to be highly complementary in that NRVS indirectly probes the structure through its vibrational behavior, whereas EXAFS reveals detailed structural parameters.[23] Here we extend this by using the NRVS vibrational analyses to provide estimates for vibrational disorder within the cluster. This in turn allows us to constrain the otherwise unknown Debye−Waller terms in the EXAFS curve fits and also to estimate the otherwise unresolved structural disorder in the cluster. Finally, DFT quantum mechanical calculations both benefit from and assist the interpretation of spectroscopic data. Together, therefore, NRVS, EXAFS, and DFT allow us both to measure the changes with oxidation state in the vibrational dynamics and structure of the Fe protein [4Fe-4S] cluster and to provide insights into the electronic origin of the observed changes.

dx.doi.org/10.1021/ja307027n | *J. Am. Chem. Soc.* 2013, 135, 2530−2543

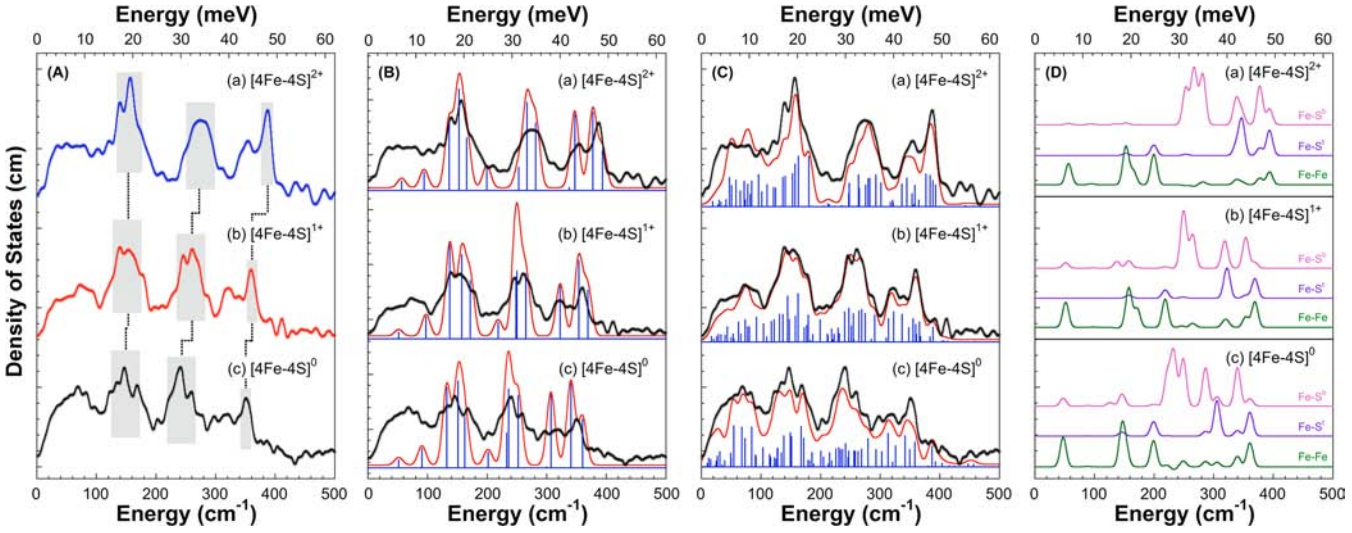

Figure 2. NRVS spectroscopy of *Av2*. (A) Comparison of the experimental NRVS-derived PVDOS spectra for different oxidation states: The shaded areas connected by vertical lines indicate shifts in band energies as discussed in the text. (B) Empirical normal-mode analyses using $Fe_4S_4(S^t)_4$ models in T_d symmetry. (C) Empirical normal-mode analyses using $Fe_4S_4(Cys)_4$ models in C_1 symmetry. (D) Decomposition of Fe−S^b (pink), Fe−S^t (violet) and Fe−Fe (green) normal modes, calculated at T_d symmetry. For each panel: (a) oxidized $[4Fe\text{-}4S]^{2+}$, (b) reduced $[4Fe\text{-}4S]^{1+}$ and (c) all-ferrous $[4Fe\text{-}4S]^{0}$. For (B) and (C) (black) experimental PVDOS data, (red) Urey−Bradley force field simulations, and (blue) corresponding stick spectra. Stick spectra correspond to individual normal-mode frequencies and their relative intensities before broadening.

Table 1. Normal Mode Decomposition with Frequencies (ν) and Intensities (e^2_{Fe}) of NRVS Spectra for the Three Oxidation Levels of Nitrogenase Fe Protein [4Fe-4S] Cluster, Simulated Using Urey−Bradley Force Field at T_d Symmetry

	oxidized $[4Fe\text{-}4S]^{2+}$					reduced $[4Fe\text{-}4S]^{1+}$					all-ferrous $[4Fe\text{-}4S]^{0}$				
mode	ν (cm^{-1})	e^2_{Fe}	Fe−S^t	Fe−S^b	Fe−Fe	ν (cm^{-1})	e^2_{Fe}	Fe−S^t	Fe−S^b	Fe−Fe	ν (cm^{-1})	e^2_{Fe}	Fe−S^t	Fe−S^b	Fe−Fe
$A_1{}^t$	393.8	0.62	46.4	26.8	23.1	369.1	0.75	42.2	13.4	41.2	360.1	0.75	42.7	13.0	42.2
$T_2{}^b$	377.2	1.21	14.0	65.5	12.1	353.8	1.20	6.4	70.4	16.8	340.6	1.30	10.1	66.3	18.5
$T_2{}^t$	347.3	1.17	65.5	20.4	4.8	322.7	0.81	59.9	7.7	6.6	305.6	1.11	63.6	15.9	8.3
$A_1{}^b$	337.7	0.05	19.2	43.3	8.7	318.2	0.00	7.5	57.4	8.0	286.4	0.01	8.6	65.7	9.6
E^b	281.6	1.04	–	85.3	5.1	264.8	1.00	–	76.3	6.7	248.9	1.22	–	81.3	10.3
$T_1{}^b$	267.1	1.35	–	94.5	–	250.0	1.04	–	81.8	–	233.0	1.25	–	91.8	–
$T_2{}^b$	253.1	0.36	2.6	61.9	–	248.5	0.94	2.5	51.0	6.5	222.2	0.58	0.5	54.5	3.3
E	165.6	0.81	–	–	23.6	171.7	0.89	–	1.0	30.1	153.0	0.66	–	0.8	26.9
$T_2{}^b$	152.8	1.56	4.3	3.3	68.5	157.5	1.29	6.8	17.1	63.9	146.2	1.24	7.4	20.6	68.3

RESULTS AND DISCUSSION

Sample Preparation and Characterization. For this study, the majority of samples were prepared in custom Lucite cuvettes that allowed NRVS, EXAFS, EPR, and Mössbauer measurements, allowing parallel experiments on the same sample. As it is essential that the Fe protein samples are prepared in pure oxidation states with negligible cluster degradation or adventitious Fe present, we used Mössbauer spectroscopy before NRVS or EXAFS experiments as detailed in the Supporting Information (SI). The zero-field Mössbauer spectra, measured at cryogenic temperatures at all three oxidation levels are in excellent agreement with earlier observations,[4] and we present typical spectra with analyses in the SI (Figure S1, Table S1). Also, it is important to note that no glassing agent, such as glycerol, was used unless we explicitly indicate otherwise. We note that it is common practice in EXAFS measurements to include such a glassing agent in order to minimize diffraction artifacts; however, as noted above, it is well established that this can modify the Fe protein cluster properties.

NRVS Results. The ^{57}Fe NRVS data for oxidized, reduced, and all-ferrous *Av2* are compared in Figure 2A. As usual, the NRVS intensities are plotted in terms of partial vibrational density of states (PVDOS). These data can be compared to our previous NRVS investigations of the $[Fe_4S_4(SPh)_4]^{2-}$ complex[24] and *Pyrococcus furiosus* (*Pf*) D14C ferredoxin (Fd)[25] as well as resonance Raman data from [4Fe-4S] clusters in model compounds and proteins[26] and oxidized *Av2*.[6,7] This allows us to group the NRVS bands into three main regions. Below 200 cm^{-1}, the intensity comes from normal modes involving torsion and breathing of the cluster, as well as motion of the entire cluster along with the peptide backbone. Between 200 and 400 cm^{-1}, one finds modes involving a mixture of Fe−S^b and Fe−S^t stretching motion, where S^b and S^t refer to bridging sulfide and terminal cysteinate sulfurs, respectively. Above 400 cm^{-1}, there are very weak features that are mostly ligand side-chain motion with a small mix of Fe−S^t stretching. Comparing the three *Av2* NRVS spectra, the general trend is that, with each reduction in oxidation level, there is a parallel decrease in the average frequencies of the Fe−S stretching modes. For example, upon one-electron reduction, the high frequency peak at 387 cm^{-1} downshifts to 359 cm^{-1} and then shifts further to 349 cm^{-1} for the all-ferrous state. In the central region, the two successive reductions shift the local maximum from 275 to 260 cm^{-1}, and from 260 to 240 cm^{-1}. For comparison, in the opposite

dx.doi.org/10.1021/ja307027n | J. Am. Chem. Soc. 2013, 135, 2530−2543

direction, oxidation of HiPIP proteins from the $[4Fe\text{-}4S]^{2+}$ to the $[4Fe\text{-}4S]^{3+}$ redox level shifts many of the Fe−S stretching modes observed by resonance Raman spectroscopy[27] by about 20 cm^{-1} to higher energy.

NRVS spectra can be simulated using an empirical parametrized force field and these calculations are presented in spectra B, C, and D of Figure 2. Complete details of the force constants used are presented in the SI (Table S2) together with detailed frequency assignments (Table S3 SI). As in previous studies of rubredoxin (Rd),[28] [2Fe-2S][29] and [4Fe-4S] Fds,[25] we began with small, high symmetry models, and then moved to larger models with lower symmetry. Spectra B and D of Figure 2 and Table 1 illustrate the results for "first draft" T_d simulations for the *Av2* spectra for each oxidation level using $[4Fe\text{-}4S](S2)_4$ models in T_d symmetry. Figure 2B contains the spectra and simulations. Table 1 is a summary of the major vibrational modes for each oxidation state together with the relative contributions from bridging Fe−S^b, terminal Fe−S^t and Fe−Fe stretching motions, while Figure 2D presents the potential energy distributions (PED) for bridging Fe−S^b, terminal Fe−S^t and Fe−Fe stretches. The T_d models yield peaks in all the regions of strong NRVS intensity, although the calculated features are sharper and more intense than the observed spectrum. This reflects the fact that, in the protein, the Fe kinetic energy is divided over a larger number of modes that also include a number of side-chain atoms and even the protein backbone. Since the PVDOS by definition integrates to 3, spreading the intensity over additional modes will weaken and broaden the spectral features. However, for comparison of force constants, the T_d simulations have a much smaller number of variables, allowing for more straightforward comparisons between samples.

Our final force field simulation results for the $[4Fe\text{-}4S](Cys)_4$ model in C_1 symmetry are presented in Figure 2C while intermediate steps for each redox level are in the SI. These more realistic simulations require inclusion of the cysteine side chains and provision for lower symmetry. Compared to the T_d simulations in Figure 2B, lowering the symmetry to D_{2d} and including 3 carbons from the cysteine side chains yielded only a modest improvement in the fit. This may reflect the fact that in D_{2d} symmetry the side-chain carbons cannot be made to closely match their true protein conformations. C_2 symmetry, in contrast, produced a marked improvement in the quality of fit, especially in the shape of features between 350−400 cm^{-1} and from 130−210 cm^{-1}. This use of C_2 symmetry is consistent with the observation from X-ray crystallography that the cluster lies on the Fe protein dimer two-fold axis.[2,3]

A comparison of the oxidized ^{57}Fe *Av2* NRVS with the significant Raman literature on [4Fe-4S] clusters[27] is instructive. We note that NRVS and resonance Raman spectroscopy are known to be highly complementary as the two techniques possess very different selection rules, and thus vibrational modes will normally have different relative intensities in NRVS and resonance Raman spectra. For example, the most intense resonance Raman band from oxidized *Av2* is at ∼338 cm^{-1} and is attributed to a totally symmetric, mostly Fe−S^b stretching mode,[6,7] while the NRVS PVDOS is very weak in this region. By contrast, the strongest feature in the corresponding NRVS spectrum in Figure 2A is in the region where S−Fe−S bending contributions predominate at ∼155 cm^{-1}, whereas the resonance Raman signal in this region is about 10-fold weaker than the Fe−S stretching region.

The highest frequency band with significant NRVS intensity has a peak at 387 cm^{-1} and is down to half intensity at 391 cm^{-1}. In an early Raman study of oxidized *Cp2*, a Raman peak at 391 cm^{-1} was assigned to an A_1 mode with mostly terminal Fe−S^t stretching character in approximate T_d symmetry,[6] and a similar band at 392 cm^{-1} is seen in oxidized *Av2*.[7] Most studies of [4Fe-4S] Fds consider the clusters in D_{2d} symmetry, but they still assign peaks in the 393−399 cm^{-1} range to A_1 modes with mostly Fe−S^t stretching character. These Raman bands are usually partially resolved from peaks in the 379−390 cm^{-1} range assigned to B_2 mode with mostly bridging Fe−S^b stretching character. Our T_d calculations predict an A_1 mostly terminal Fe−S^t stretching mode at 393 cm^{-1}. Thus, it is straightforward to assign our observed NRVS band at 387 cm^{-1} to an unresolved combination of these Fe−S^t and Fe−S^b stretching modes. Figure S3 in the SI illustrates these modes. Establishing the symmetric terminal Fe−S^t stretching frequency is relevant to the understanding of redox-induced changes in force constants.

Another important mode for defining force constants is the mostly bridging Fe−S^b A_1 stretch, which occurs as the strongest band in the resonance Raman spectrum at 335 or 337 cm^{-1}, respectively, for *Cp2*[6] or *Av2*.[6] Our T_d calculation posits a band at 337 cm^{-1} with virtually no intensity, and this is because the mode is almost pure S^b motion with very little involvement of the Fe atoms. In the experimental data there is a small amount of intensity in this region, presumably because of somewhat more Fe motion in the lowered symmetry of the protein. Such dramatic differences between NRVS intensity and resonance Raman intensity have been seen before, in the ∼314 cm^{-1} Fe−S symmetric stretch for Rd,[28] and the 315 cm^{-1} Fe−S^b stretch in [2Fe-2S] Fds.[29]

The other major features in the NRVS are a strong band at 274 cm^{-1} and a set of peaks at 120, 136, and 156 cm^{-1}. The 274 cm^{-1} band corresponds to [4Fe-4S] Fd Raman bands assigned to Fe−S^b stretching modes. The modes between 120 and 156 cm^{-1} are Fe−S bending in character and actually the strongest features in the spectrum. Although rarely reported, Raman bands in this 120−160 cm^{-1} region can also be observed.[25] Finally, the NRVS has intensity between 30 cm^{-1} and 100 cm^{-1}, which presumably spans torsional modes and motions involving extensive motion of the polypeptide. These are difficult to observe by other techniques.

For reduced *Av2*, resonance Raman spectra have not been measured, and apart from our recent study of *Pf* Fd,[25] these are the only data on the vibrational dynamics of a reduced $[4Fe\text{-}4S]^{1+}$ cluster. We can use the simulations in Figure 2 and Table 1 to estimate the location of key features. Specifically, the T_d calculations predict the A_1 mostly terminal Fe−S^t stretching modes at 369 cm^{-1} with modest intensity and the mostly Fe−S^b A_1 stretch at 318 cm^{-1} with virtually no intensity. Such band shifts are consistent with our recent observation on *Pf* D14C Fd. In general, the predicted locations of the totally symmetric modes vary by ±5 cm^{-1} for calculations with different symmetries. The ∼6% band shifts with reduction are relatively small compared with the 18% (65 cm^{-1}) downshifts seen in Rd Fe−S frequencies.[28]

For the all-ferrous state, resonance Raman spectra are also unavailable and are unlikely to be measured as this oxidation state is not strongly colored. Hence, these NRVS data comprise the first vibrational data on the $[4Fe\text{-}4S]^0$ state. Similar to oxidized and one-electron-reduced *Av2*, all-ferrous *Av2* shows three distinct regions in NRVS spectrum. As expected, there is

further downshift of PVDOS features upon further reduction. Scott and co-workers observed a 0.7% increase in the core volume upon reduction in the $[Fe_4S_4(CN)_4]^{4-}$ model complex from $[Fe_4S_4(CN)_4]^{3-}$, and they concluded that the additional electron is described by an "antibonding orbital with substantial sulfur character".[15] The T_d calculations predict the A_1 mostly terminal Fe–S^t stretching modes at 360 cm^{-1} with modest intensity and the mostly bridging Fe–S^b A_1 stretch at 300 cm^{-1}, the latter again with virtually no NRVS intensity. There is also a significant shift for the 274 cm^{-1} peak of oxidized *Av*2 to 240 cm^{-1} in the all-ferrous state. Although a decrease in NRVS intensity is noticeable in the 120–160 cm^{-1} region in the all-ferrous state, no significant red shift is observed. The overall splitting of features in the 150 cm^{-1} range becomes even larger in the two-electron-reduced state. NRVS calculations for T_d, D_{2d}, C_2, and C_1 symmetry models are detailed in the SI (Figure S2).

We summarize the variation in calculated Fe–S stretching force constants as a function of the average Fe oxidation state in Figure 3. For comparison, we include data from previous work

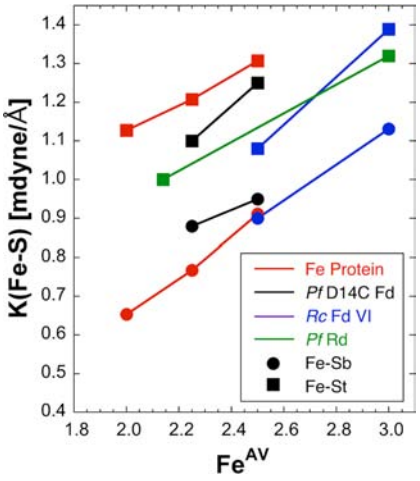

Figure 3. Overall trends in Fe–S stretching constants from NRVS for bridging sulfides (●) and terminal thiolates (■) as functions of average Fe oxidation state, Fe^{AV}. (red) Fe protein, (black) *Pf* D14C Fd,[25] (blue) [2Fe-2S] containing *Rc* Fd VI,[29] (green) *Pf* rubredoxin.[28]

on the mononuclear $Fe(SCys)_4$ site in *Pf* Rd,[28] the $[2Fe\text{-}2S](SCys)_4$ cluster in *Rhodobacter capsulatus* (*Rc*) Fd VI,[29] and the $[4Fe\text{-}4S](SCys)_4$ cluster in *Pf* D14C Fd.[25] Inspection of this figure clearly shows the stepwise increase in K(Fe–S) with oxidation states for both Fe–S^b and Fe–S^t modes. The Fe–S^b values from the bridging sulfides show a consistent linear trend, which for the limited data in Figure 3 would fit well to a straight line. The Fe–S^t values from the terminal cysteine thiolates also show a stepwise increase with oxidation state; however, there is more variation in absolute value between proteins. This presumably reflects the greater impact of the polypeptide environment on these modes as they include the amino acid cysteine, while the vibrations from the bridging sulfides are perhaps more an inherent property of the cluster. Nevertheless, the terminal Fe–S^t modes consistently show stronger force constants than the bridging Fe–S^b modes, consistent with the greater strength of the Fe–S^t bond compared to that of the the cluster core bonds. This stepwise shift with oxidation state is also clearly apparent in the individual PED contributions plotted in Figure 2D for the Fe–S modes. A similar shift is seen with the Fe–Fe modes. Interestingly, inspection of Table 1 reveals that, while the energy of each mode tends to decrease with each reduction, there is no concomitant systematic change in the composition of each mode in terms of Fe–S^t, Fe–S^b, and Fe–Fe contributions.

Finally, we note that the NRVS analysis is significantly assisted by the availability of the EXAFS analysis below and vice versa. For NRVS, the detailed structural parameters provided by EXAFS can be used to refine the models used for the force-field analysis. This is illustrated for the all-ferrous state in Figure S4 in the SI, where there is improvement in the fit as our structural model was refined. Similarly, for EXAFS, the detailed understanding from NRVS of the vibrational structure of the [4Fe-4S] cluster in Fe protein can greatly assist in the analysis of the corresponding EXAFS spectra. An important and often unknown variable in EXAFS curve-fitting analyses is the Debye–Waller factor for each interaction. The Debye–Waller factor is a measure of the overall variation, or disorder, in interatomic distance. It can be separated into two components: the "static" variation arising from structural inhomogeneity and the "dynamic" variation from interatomic vibrations. As ambiguities in the Debye–Waller factors can cause major uncertainties in EXAFS analysis, it is essential to obtain good estimates of these terms.[30] In the early days of EXAFS, Debye–Waller factors were often estimated from model compound measurements or just allowed to float between reasonable values. More recently there has been significant progress in estimating dynamic Debye–Waller terms,[30] and empirical methods based on force-field models have been developed[31] along with more generally applicable ab initio approaches.[32] Here, we can use our analysis of the [4Fe-4S] vibrational structure from NRVS measurements to directly calculate the dynamic disordered Debye–Waller term. As summarized by Cyvin,[33] the assumption of a harmonic oscillator model for each normal mode provides an estimate of the mean square deviation (σ^2) for particular interatomic distances in that mode at a specific temperature. The overall σ^2 for that distance, then, is the sum of such contributions over all modes. Hence, for the Fe protein NRVS data here using T_d symmetry and a temperature of 10 K we estimate σ^2_{Fe-S} to be between 0.00235 and 0.00307 $Å^2$ for the Fe–S interactions, with σ^2_{Fe-Fe} between 0.00237 and 0.00261 $Å^2$ for the Fe–Fe interactions. These values provide an important constraint for the equivalent parameters used in EXAFS curve fitting. In addition, the ability to estimate vibrational disorder also means that a combined EXAFS and NRVS experiment should allow an estimate of structural, or static, disorder (σ^2_{stat}) by subtracting the total σ^2 determined from EXAFS from the vibrational σ^2_{vib} from NRVS. These aspects, and detailed significance of the calculated values are discussed below in the context of our EXAFS analysis.

EXAFS Results. Our new Fe EXAFS data and simulations for *Av*2 at different oxidation levels are illustrated in Figure 4. An essential feature of these new measurements is that no glassing agent, such as glycerol, was used unless we explicitly indicate otherwise. EXAFS has been reported previously by Lindahl et al.,[9] Ryle et al.,[8] Musgrave et al.,[11] and recently by Blank et al.[10] Our data are similar, except that a decade in progress of synchrotron radiation sources and detectors allowed us to take spectra over a wider range, that is out to k = 16 or 21 $Å^{-1}$ as opposed to 14 $Å^{-1}$ or less in previous studies. The EXAFS curve-fitting parameters are presented in Table 2, while Table 3 compares the interatomic distances derived from selected EXAFS fits, XRD, and DFT, with associated root-

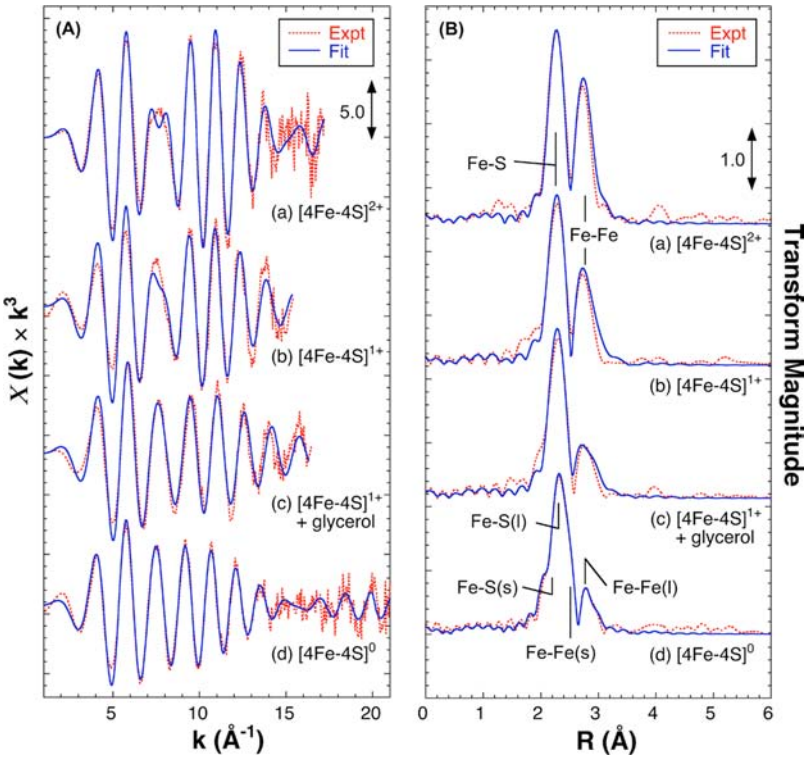

Figure 4. EXAFS spectra (A: left) and Fourier transforms (B: right) for *Av2* in different oxidation levels. For each panel: (a) oxidized $[4Fe\text{-}4S]^{2+}$; (b) reduced $[4Fe\text{-}4S]^{1+}$; (c) reduced $[4Fe\text{-}4S]^{1+}$ with 15% glycerol; (d) all-ferrous $[4Fe\text{-}4S]^{0}$. For each plot: (red ---) spectrum; (blue ——) simulation. Fourier transforms are phase-shift corrected using sulfur as the backscattering atom. The fits in (c) and (d) use the parameters in Table 2 from (c1) and (d3), respectively.

mean-square (RMS) deviations derived from EXAFS, NRVS, XRD, and DFT. As seen by others, Fourier transforms comprise two strong peaks for Fe−S and Fe−Fe interactions, and very little else. From the EXAFS data shown in Figure 4, we conclude that oxidized and reduced *Av2* clusters have similar geometries. On the other hand, the Fe−Fe peak in the all-ferrous data is greatly diminished, as seen previously.[11] A similar quenching of the Fe−Fe interaction is also seen in the reduced state when 15% glycerol is present. For quantitative analysis, our curve-fitting approach was to start with single Fe−S and Fe−Fe components, fixing the number (N) of Fe−S and Fe−Fe interactions to the expected values for a single Fe site, namely 4 and 3, respectively. The variables were then the Fe−S and Fe−Fe distances (R) and the variance or mean square deviations in those distances (σ^2_{Fe-S} and σ^2_{Fe-Fe}) that are part of the associated Debye−Waller factors ($\exp(-2\sigma^2k^2)$) in the EXAFS equation. Where necessary, we constrained the variances to be consistent with those calculated from NRVS results. Note that in this discussion we will quote RMS deviations in distance (σ) as opposed to the more usual mean square deviations (σ^2) since the former allows a more intuitive connection to familiar interatomic distances.

The oxidized *Av2* EXAFS (Figure 4, plots a) exhibits the strongest Fe−Fe peak in its Fourier transform, indicating the most ordered shell of Fe−Fe distances among the *Av2* samples. A 2-shell fit (a) (Table 2 and Table 3) gave an average Fe−S distance of 2.286 Å and an average Fe−Fe distance of 2.72 Å, with total σ of 0.059 Å and 0.067 Å, respectively. Using the NRVS tetrahedral simulations to estimate the respective dynamic disorders (σ_{vib}) as 0.050 Å and 0.051 Å, we calculate the respective static contributions (σ_{stat}) to disorder for the Fe−S and Fe−Fe shells as 0.031 and 0.043 Å (Table 3). Thus, although it is chemically reasonable to assume different Fe−S distances for bridging sulfide and cysteine thiolate sulfurs, the difference is likely less than the experimental resolution of ∼0.10 Å. For comparison, in the atomic resolution (0.92 Å) *Bacillus thermoproteolyticus* (*Bt*) Fd structure, average Fe−S^b and Fe−S^t distances were 2.291 and 2.278 Å, respectively.[34] The EXAFS prediction for the *Av2* Fe−Fe distance was 2.72 Å. Although longer than the average X-ray diffraction values of 2.66 Å and 2.63 Å from the 2.2 and 1.93 Å resolution *Av2* and *Cp2* structures,[2] the prediction is similar to typical average values reported for $[4Fe\text{-}4S]^{2+}$ clusters in model compounds, such as 2.722 Å in $(Bu_4N)_2[Fe_4S_4(SC_6H_5)_4]$[35] or 2.736 Å in $(Me_4N)_2[Fe_4S_4(SC_6H_5)_4]$.[36] It also compares well with average Fe−Fe distances in high-resolution Fd structures. For example, the *Bt* Fd form 1 structure had average Fe−Fe distances of 2.725 Å with σ = 0.025 Å,[34] whereas *Clostridium acidurici* Fd clusters I and II had average Fe−Fe distances of 2.726 Å (±0.032 Å) and 2.722 (±0.019 Å), respectively.[37] In summary, the EXAFS indicates a reasonably symmetric cluster with modest distortions typical of other routine Fds.

The reduced *Av2* EXAFS (Figure 4, plots b) exhibit a Fourier transform very similar to those of the oxidized data, with a slightly smaller Fe−Fe peak, indicating a more disordered shell of Fe−Fe distances. However, 2-shell fits (b) in Table 2 and Table 3 were still adequate, in this case giving an average Fe−S distance of 2.295 Å and the same average Fe−Fe distance of 2.72 Å. In this case the RMS deviation for the Fe−Fe distances of 0.083 Å is consistent with the smaller Fe−Fe peak, and again by using the NRVS measurement to estimate the dynamic component, σ_{vib}, we calculate a slightly larger RMS static disorder of Fe−Fe distances of 0.067 Å. This additional disorder is consistent with small-molecule structures, whereas if

dx.doi.org/10.1021/ja307027n | J. Am. Chem. Soc. 2013, 135, 2530−2543

Table 2. EXAFS Curving-Fitting Parameters[a]

	Fit	Interaction	N	R (Å)	σ^2 (Å^2)	σ (Å)	ΔE_0 (eV)	ΔR (Å)	F
Oxidized $[4Fe\text{-}4S]^{2+}$	(a)	Fe-S	4	2.286 (1)	0.0035 (1)	0.059	-11.9 (4)	0.097	0.262
		Fe-Fe	3	2.720 (2)	0.0045 (1)	0.067			
Reduced $[4Fe\text{-}4S]^{1+}$	(b)	Fe-S	4	2.295 (2)	0.0040 (1)	0.063	-12.0 (4)	0.110	0.323
		Fe-Fe	3	2.721 (3)	0.0068 (2)	0.083			
Reduced $[4Fe\text{-}4S]^{1+}$ + Glycerol	(c0)	Fe-S	4	2.309 (2)	0.0042 (1)	0.064	-12.8 (4)	0.105	0.297
		Fe-Fe	3	2.723 (5)	0.0118 (5)	0.109			
	(c1)	Fe-S	4	2.301 (3)	0.0047 (7)	0.068	-15.7 (6)	0.105	0.285
		Fe-Fe (short)	1	2.508 (6)	0.0064 (7)	0.080			
		Fe-Fe (long)	2	2.708 (5)	0.0060 (3)	0.077			
All-Ferrous $[4Fe\text{-}4S]^{0+}$	(d0)	Fe-S	4	2.322 (2)	0.0055 (1)	0.074	-13.2 (5)	0.083	0.256
		Fe-Fe (short)	1.5	2.555 (5)	0.0075 (5)	0.086			
		Fe-Fe (long)	1.5	2.756 (4)	0.0047 (2)	0.068			
	(d1)	Fe-S (short)	1	2.232 (5)	0.0040 (4)	0.063	-13.1 (5)	0.083	0.252
		Fe-S (long)	3	2.332 (2)	*0.0031*	0.055			
		Fe-Fe (short)	0.5	2.551 (3)	0.0015 (2)	0.038			
		Fe-Fe (long)	2.5	2.740 (4)	0.0098 (4)	0.098			
	(d2)	Fe-S (short)	1	2.216 (5)	0.0036 (3)	0.060	-15.1 (5)	0.083	0.246
		Fe-S (long)	3	2.324 (2)	*0.0031*	0.055			
		Fe-Fe (short)	1	2.551 (4)	0.0034 (2)	0.058			
		Fe-Fe (long)	2	2.737 (4)	0.0065 (2)	0.081			
	(d3)	Fe-S (short)	1	2.213 (5)	0.0033 (2)	0.057	-15.8 (5)	0.083	0.246
		Fe-S (long)	3	2.324 (3)	*0.0031*	0.056			
		Fe-Fe (short)	1.5	2.562 (4)	0.0058 (3)	0.076			
		Fe-Fe (long)	1.5	2.748 (4)	0.0043 (2)	0.065			
	(d4)	Fe-S (short)	1	2.216 (5)	0.0031 (2)	0.055	-16.0 (6)	0.083	0.248
		Fe-S (long)	3	2.327 (3)	*0.0031*	0.055			
		Fe-Fe (short)	2	2.570 (5)	0.0097 (5)	0.098			
		Fe-Fe (long)	1	2.759 (3)	0.0028 (1)	0.052			

[a]Shading indicates the final fits used in Figure 5 (see text). N = number of backscattering atoms used in EXAFS fit; R = distance used in EXAFS fit; σ^2 = mean-squared deviation (Debye−Waller factor) used in fit; σ = equivalent root-mean-squared deviation (Debye−Waller factor); ΔE_0 = offset in E_0; ΔR = EXAFS resolution from k-range; F = EXAFS fit quality = $\sqrt{[\Sigma(\chi_o - \chi_c)^2 k^6/\Sigma\chi_o^2 k^6]}$ where χ_o = observed EXAFS; χ_c = calculated EXAFS. Fixed parameters are in italics. Figures in parentheses are the standard deviations for each fitted parameter. Phases and amplitudes were calculated using FEFF 7.0. The scale factor used was 0.85.

we look at the variation of Fe−Fe distances in reduced [4Fe-4S]$^{1+}$ clusters, there is often, but not always, more disorder.[38] Several groups have remarked on the additional "plasticity" of reduced core structures.[38] Finally, in the 1GSP crystal structure (an initially dithionite-reduced sample), the average Fe−Fe distance is 2.66 Å with a RMS deviation of 0.053 Å,[2] midway between the disorder predicted from the EXAFS for the oxidized and reduced samples. Thus, the disorder predicted by the combined application of NRVS and EXAFS is in good agreement with the protein crystallography, and that is quite gratifying, considering the chain of approximations and multiple measurements involved. The EXAFS average Fe−Fe distance of 2.72 Å is again somewhat longer than the crystallographic 2.66 Å distance,[3] but closer to the 2.68 Å average distance reported in the PDB for 41 [4Fe-4S] structures.

The impact on the EXAFS spectrum of adding glycerol deserves some comment, and data from a sample with 15% glycerol are presented in Figure 4, plot c. It is clear that the Fe−Fe interaction is substantially quenched compared to that of the sample without glycerol, indicating a greatly increased heterogeneity in the Fe−Fe distance. This is reflected in the curve-fit analysis. A 2-shell fit (c0 in Table 2) still gives an Fe−Fe distance of 2.72 Å, but now with an unrealistically high σ of 0.109 Å that is about the same as the resolution of the EXAFS spectrum. A better fit was obtained by splitting the Fe−Fe interaction into 2 subshells, with 1 short and 2 long Fe−Fe interactions at 2.51 Å and 2.71 Å, respectively (c1 in Table 2) with the a single Fe−S at 2.30 Å. Since EXAFS analysis yields the average coordination sphere for a single Fe, this 1:2 Fe:Fe ratio would imply 2 of the 6 Fe−Fe distances in the [4Fe-4S] cubane are short, while the other 4 are long. However, both

dx.doi.org/10.1021/ja307027n | J. Am. Chem. Soc. 2013, 135, 2530−2543

Table 3. Interatomic Distances Derived from EXAFS, XRD, and DFT with Associated RMS Deviations Derived from EXAFS, NRVS, XRD, and DFT[a]

			interatomic distance, R (Å)			RMS deviation in distance, σ (Å)				
	interaction	N	EXAFS	XRD (mean)	DFT (mean)	EXAFS (total)	NRVS (dynamic)	EXAFS − NRVS (structural)	XRD (structural)	DFT (structural)
oxidized $[4Fe\text{-}4S]^{2+}$ (a)	Fe−S	4	2.286	2.30 (a)	2.30	0.059	0.050	0.031	0.030 (a)	0.047
				2.32 (b)					0.018 (b)	
	Fe−Fe	3	2.720	2.63 (a)	2.69	0.067	0.051	0.043	0.057 (a)	0.007
				2.66 (b)					0.053 (b)	
reduced $[4Fe\text{-}4S]^{1+}$ (b)	Fe−S	4	2.295	2.30 (a)	2.31	0.063	0.053	0.035	0.030 (a)	0.037
				2.32 (b)					0.018 (b)	
	Fe−Fe	3	2.721	2.63 (a)	2.63	0.083	0.049	0.067	0.057 (a)	0.051
				2.66 (b)					0.053 (b)	
all-ferrous $[4Fe\text{-}4S]^{0}$ (d0)	Fe−S	4	2.322	2.32 (c)	2.37	0.074	0.055	0.050	0.025 (c)	0.037
	Fe−Fe (short)	1.5	2.562	2.57 (c)	2.57	0.086	0.051	0.070	0.046 (c)	0.009
	Fe−Fe (long)	1.5	2.748	2.72 (c)	2.75	0.068		0.046	0.052 (c)	0.026
all-ferrous $[4Fe\text{-}4S]^{0}$ (d3)	Fe−S (short)	1	2.213	2.32 (c)	2.32	0.057	0.055	0.019	0.025 (c)	0.024
	Fe−S (long)	3	2.324		2.39	0.056		0.010		0.021
	Fe−Fe (short)	1.5	2.562	2.57 (c)	2.59	0.076	0.051	0.057	0.046 (c)	0.009
	Fe−Fe (long)	1.5	2.748	2.72 (c)	2.75	0.065		0.041	0.052 (c)	0.026

[a] N = number of interactions per Fe. The EXAFS − NRVS (structural) column was calculated using $\sqrt{(\sigma^2_{EXAFS} - \sigma^2_{NRVS})}$. XRD values were derived from PDB structures (a) 1CP2, (b) 1G5P, (c) 1G1M. Note the oxidation states of (a) and (b) are ambiguous as discussed in the main text.

Fe−Fe interactions still have significant σ in the region of 0.08 Å, indicating significant further unresolved disorder within the cluster. Clearly, the presence of 15% glycerol can substantially affect the conformational structure of the cluster.

Our results contrast with a recent study by Blank and co-workers, who reported the EXAFS spectrum of reduced *Av*2 containing 50% glycerol in addition to dithionite.[10] This spectrum shows significantly greater Fe−Fe intensity in the Fourier transform compared with the data in Figure 4, plot c. Interestingly, these workers also fitted this spectrum in terms of a single Fe−S interaction at 2.30 Å and a 1:2 ratio of distinct Fe−Fe distances of 2.50 and 2.72 Å. However, the 2.50 Å Fe−Fe interaction has an unrealistically high σ of 0.113 Å and consequently contributes less than 3% of the EXAFS intensity. Hence, this spectrum is better fitted to a single Fe−Fe interaction, which gives a distance of 2.72 Å and σ in the region of 0.08 Å, a result similar to our *Av*2 data measured without glycerol present. Interestingly, this study also includes EXAFS of the Fe proteins from the alternative vanadium and iron-only nitrogenase in 50% glycerol, and these do show spectra and analyses similar to those of our sample with 15% glycerol.

The all-ferrous *Av*2 EXAFS in Figure 4, plot d, exhibits a rather different Fourier transform from the spectra of other oxidation states, and a more complex model is required to simulate the *k*-space EXAFS data. Because of the paucity of data about [4Fe-4S] clusters at this oxidation level, we recorded the spectrum out to k = 21 Å^{-1}, a wider range than normally achieved for Fe K-edge EXAFS. This yielded the better resolution of 0.087 Å. Whereas 2-shell fits were adequate for the oxidized and reduced EXAFS simulations, for a good fit to the all-ferrous data, it was necessary to split both the Fe−S and Fe−Fe shells into 2 subshells.

For the Fe−S interaction, fits that included only a single Fe−S shell (for example, d0 in Table 2) gave a significantly poorer quality fit as well as a larger σ of 0.074 Å for this interaction. In particular, the higher *k*-region of the EXAFS did not fit well. Including a single, shorter Fe−S interaction substantially improved the quality of the fit and reduced the σ to 0.057 Å. In fact it was necessary to constrain σ for the longer Fe−S interaction to ensure it was greater or equal to the 0.056 Å (equivalent to σ^2 = 0.0031 Å^2) calculated from the NRVS measurements.

For the Fe−Fe interaction, we investigated a number of fits ranging from 0.5 to 2.0 short Fe−Fe contributions, and examples are presented in Table 2. We found that the best fit was provided by 1.5 of each interaction per Fe at 2.56 Å and 2.75 Å, giving approximately similar σ of 0.076 Å and 0.066 Å, respectively (Table 3, (d3)). This is consistent with the [4Fe-4S] cluster having a 3:3 ratio of shorter and longer Fe−Fe interactions. The fit with 1 short Fe−Fe and 2 longer Fe−Fe interactions at 2.55 Å and 2.74 Å was similar in quality but had more dissimilar σ of 0.058 Å and 0.081 Å, respectively (d2 in Table 2). The fits with 2 shorter Fe−Fe distances or just 0.5 short Fe−Fe not only reduced the fit quality but also required unrealistically high σ of around 0.1 Å for the majority of Fe−Fe interactions (d1 and d4 in Table 2). Finally, we note that if we constrained σ to be equal for both Fe−Fe interactions, the fit yielded 1.68 long Fe−Fe to 1.31 short Fe−Fe with the quite reasonable σ for Fe−Fe of 0.07 Å (not shown). In summary our EXAFS results suggest that the all-ferrous state is distorted with equal amounts of long and short Fe−Fe interactions, but a model with 1 shorter and 2 longer Fe−Fe interactions cannot be excluded.

This conclusion is contrary to that reported by Musgrave et al.[11] who suggested two 2.53 Å and 2.77 Å Fe−Fe distances in a 2:1 ratio. These workers also commented on increased Fe−S distance to 2.36 Å, whereas our data suggest a split Fe−S shell, with a 3:1 ratio of 2.32 Å and 2.21 Å Fe−S distances. We note that the improved resolution of our experiment, with EXAFS measured up to k = 21 Å^{-1}, has allowed a much more precise

dx.doi.org/10.1021/ja307027n | J. Am. Chem. Soc. 2013, 135, 2530−2543

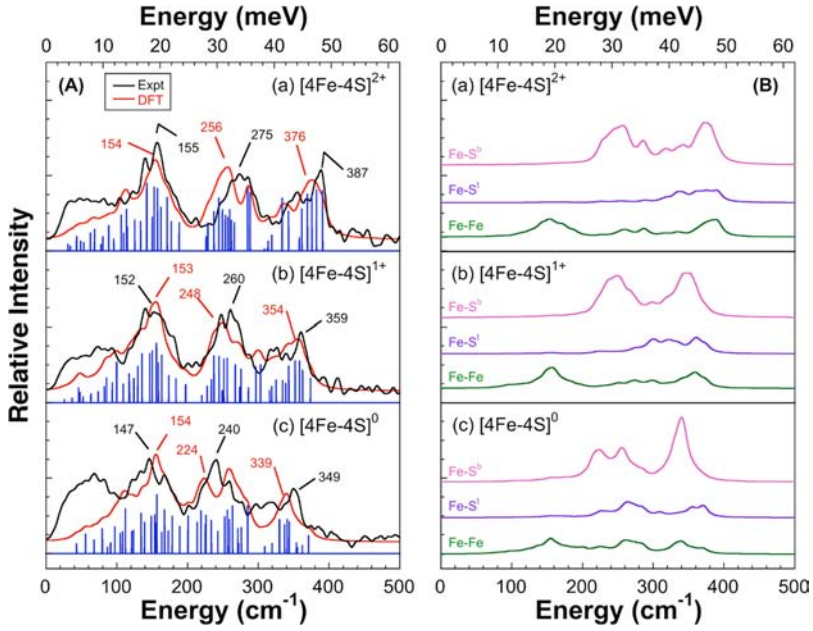

Figure 5. (A) Comparison of (black) experimental and (red) DFT calculated *Av2* PVDOS in the three oxidation states. The (blue) "stick" spectra indicate individual modes from the DFT calculations. (B) The corresponding calculated potential energy distribution (PED) profiles for (pink) Fe−S^b, (violet) Fe−S^t, and (green) Fe−Fe stretching modes. For each panel: (a) oxidized $[4Fe\text{-}4S]^{2+}$; (b) reduced $[4Fe\text{-}4S]^{1+}$; (c) all-ferrous $[4Fe\text{-}4S]^0$.

analysis, to the point where both Fe−Fe interactions are apparent in the Fourier transform spectra; the 2.74 Å distance is present as a well-defined peak, while the 2.55 Å interaction can be seen as a subtle shoulder on the side of the intense 2.32 Å Fe−S band. This is indicated in Figure 4, plot d, but is most apparent in the component breakdown presented in Figure S6 in the SI. The SI also includes the component breakdown for the reduced state for comparison in Figure S5.

These results can be compared with the known all-ferrous model [4Fe-4S] clusters with capping cyanide[15] or carbene[16] ligands. The model with 1.5 short and 1.5 long Fe−Fe interactions would be consistent with a structure such as in the carbene model. In that structure, the average Fe−Fe distance of 2.680 Å derives from 6 individual Fe−Fe distances spanning from 2.603 to 2.764 Å with RMS deviation σ = 0.063 Å. For EXAFS purposes these interactions can be split into two subgroups with average distances of 2.63 and 2.73 Å, with respective subgroup σ of 0.04 and 0.03 Å, respectively. The model with 1 short and 2 long Fe−Fe interactions would be more consistent with a structure such as in the cyanide complex. Thanks to its C_2 symmetry, this cluster has only 4 unique Fe−Fe distances, 1 each at 2.627 and 2.696 Å and 2 each at 2.676 and 2.683 Å, and hence an average of 2.673 Å.

Finally, we can again use our EXAFS RMS deviation to estimate the degree of static disorder in the [4Fe-4S] cluster. Using the NRVS T_d simulations to estimate the dynamic disorder (σ_{vib}) of the Fe−Fe shells as 0.051 Å, we calculate the static contributions (σ_{stat}) for the long and short Fe−Fe shells as 0.041 and 0.057 Å, not too dissimilar from the 0.052 Å and 0.057 Å from the crystal structure (Table 3). The agreement from the Fe−S shells is less good, in particular because the shorter Fe−S interaction is not apparent in the crystal structure. Using the single-shell Fe−S fit we calculate an overall static disorder of 0.05 Å, which is significantly greater than the 0.025 Å variation in the crystal structure.

DFT Results. As a complement to the NRVS and EXAFS experiments, we have performed DFT calculations to investigate the dynamics and structures of the *Av2* [4Fe-4S] cluster in all three oxidation levels. DFT provides a good qualitative and reasonable quantitative insight into the vibrational dynamics of Fe−S systems, and we have used it previously to help interpret the NVRS of clusters such as the nitrogenase FeMo cofactor,[39] $[Fe_4S_4(SPh)_4]^{2-}$ complex,[24] and *Pf* D14C Fd.[25] Our broken-symmetry (BS) DFT calculations as detailed below and in the methods section (SI) also provide structural parameters for comparison with EXAFS measurements, as well as insights to the electronic origin of structural changes in the [4Fe-4S] cluster with respect to oxidation state.

Collinear ("up", "↑"; or "down", "↓") spin coupling of the four Fe sites of the cluster was applied to produce proper BS states at the three oxidation levels.[25,40] The following spin coupling patterns and spin projection (M_S) configurations were used: [2Fe↑:2Fe↓], M_S = 0, for the oxidized $[4Fe\text{-}4S]^{2+}$; [2Fe↑:2Fe↓], M_S = 1/2, for the reduced $[4Fe\text{-}4S]^{1+}$; [3Fe↑:1Fe↓], M_S = 4, for the all-ferrous $[4Fe\text{-}4S]^0$. The applicability of this setup for the oxidized (total spin S = 0), reduced (S = 1/2), and all-ferrous (S = 4) [4Fe-4S] clusters was earlier discussed in the literature.[17,18] The self-consistent field (SCF) BS solutions bear a mixed-valence character common for iron−sulfur clusters, however retaining the initially assigned site spin directions. For the oxidized and reduced [4Fe-4S] 6 such BS patterns are available, and 4 for the all-ferrous oxidation level. For the oxidized $[4Fe\text{-}4S]^{2+}$ cluster, we received a solution named BS*34* after the spin-up (↑) Fe numbers *3* and *4*, as found in the 2NIP PDB file.[2] Similarly, for the reduced $[4Fe\text{-}4S]^{1+}$ cluster, the most favorable solution found was BS14. For the all-ferrous $[4Fe\text{-}4S]^0$ level, we obtained BS123, with the spin-up Fe site numbers corresponding to the 1G1M PDB file.[3] However, only a marginal energy difference within 1 kcal/mol between the geometry optimized BS states was obtained for each oxidation level.

The NRVS spectra modeled by DFT for the three oxidation levels of *Av2* are summarized in Figure 5. The overall shapes of the experimental vs calculated spectral lines are in good

dx.doi.org/10.1021/ja307027n | J. Am. Chem. Soc. 2013, 135, 2530−2543

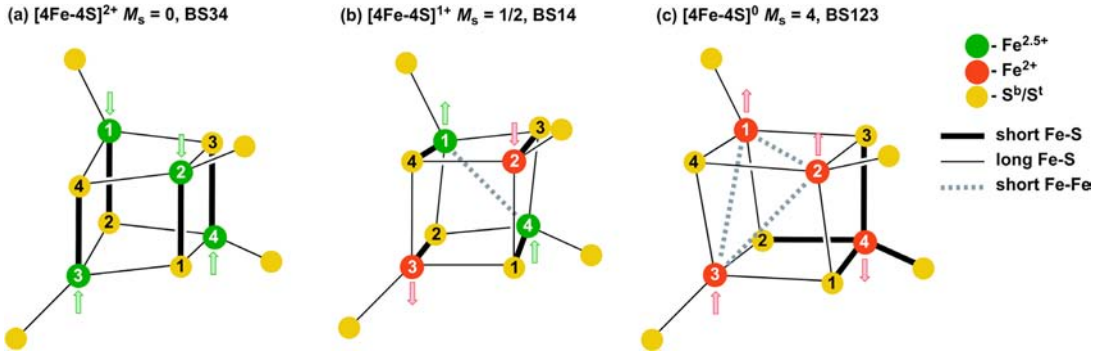

Figure 6. Schematic interrelationship of Fe−S bond lengths and Fe−Fe distances with spin polarization in the [4Fe-4S] cluster as obtained from DFT optimizations. (a) oxidized $[4Fe\text{-}4S]^{2+}$; (b) reduced $[4Fe\text{-}4S]^{1+}$; (c) all-ferrous $[4Fe\text{-}4S]^{0}$. For each structure the spin-state (M_S) and the broken symmetry pattern (BS) are indicated, while the arrows show spin direction for each Fe site. Atom numbering follows PDB files 2NIP and 1G1M.

accordance, providing an offset between the major peak positions within 20 cm^{-1}, and typically much less. With our choice of DFT methods these peak frequencies are generally lower than those observed. As in our earlier studies,[25] the three major bands seen experimentally (e.g., those centered at 387, 275, and 155 cm^{-1} in the oxidized form) can be easily matched to the corresponding computed features.

Figure 5 includes DFT calculated potential energy distribution (PED) profiles for the Fe−S^t, Fe−S^b and Fe−Fe stretching modes that facilitate the analysis of the NRVS spectra. The PEDs confirm what has been deduced empirically; that Fe−S stretching modes are located above 200 cm^{-1}, while the area below 200 cm^{-1} contains Fe−Fe stretching or, equivalently[39] S−Fe−S bending modes. The PEDs from DFT and force field simulations correspond well, as depicted in Figure 2D above. The origin of the lowest energy bands as S−Fe−S bends is revealed by the significant Fe−Fe PED with little of Fe−S^t or Fe−S^b stretching character. The DFT calculations also confirm that the highest frequency Fe−S stretching modes, found around 390 cm^{-1} for the oxidized $[4Fe\text{-}4S]^{2+}$ form, have the most terminal Fe−S^t character although they also clearly have significant bridging Fe−S^b contributions. At intermediate frequencies around 270 cm^{-1}, the vibrational energy appears to be dominated by bridging Fe−S^b stretches from the 12 Fe−S^b bonds with little intensity in the Fe−Fe PED.

Another interesting result from the DFT calculations is the change in character of the Fe−S stretching modes upon stepwise reduction of the cluster. The stepwise decrease in Fe−S stretching frequencies upon addition of electrons is consistent with trends in the bond lengths of the optimized structures, as we discuss below in the context of the EXAFS results. It is also consistent with the empirical K(Fe−S) force constants derived from NRVS and presented in Figure 3. For the oxidized cluster, the PED diagram shows that Fe−S^t stretching is primarily localized in the modes between 300−400 cm^{-1}. With one electron reduction, the Fe−S^t stretching mode region is more delocalized and shifted by about 25 cm^{-1} to lower frequencies. For the all-ferrous state, the shape of the terminal Fe−S^t PED profile more closely maps that of the bridging Fe−S^b PED, suggesting a more homogeneous involvement of the terminal and bridging sulfur types in the vibrational dynamics in this highly reduced oxidation state. In contrast to the Fe−S modes, Fe−Fe stretchings (or S−Fe−S bendings) localization is nearly invariant with respect to the [4Fe-4S] oxidation level: the corresponding major PVDOS peak centers in Figure 5 remain within the 153−154 cm^{-1} area from DFT, and within 147−155 cm^{-1} from the NRVS experiment.

We now consider the optimized structures provided by DFT calculations. To assess the effects of the cysteine positioning and protein environment at each [4Fe-4S] oxidation level, we optimized the $[4Fe\text{-}4S](SCH_2CH_3)_4$ model using three scenarios. In the representative scenario (i), also used for the NRVS modeling described above, the solvent effects are included and four cysteine Cα carbons are fixed to their XRD positions; in scenario (ii) the solvent effects are omitted; and further in scenario (iii) we also release the fixations of Cα. An important result invariant to these three (i−iii) scenarios is that the optimized Fe−Fe and Fe−S distances commonly fall into the same "short/long" groups governed by particular BS spin configuration and the oxidation level as illustrated in Figure 6, Table 4 and Table S4 of the SI. The distance ranges however can overlap between the groups as described below. A systematic rationalization of these groups, similar to those obtained by Torres et al earlier,[18] would involve careful analysis of antiferromagnetic coupling and spin-dependent delocalization[19,40,41] which goes beyond the scope of this paper; a recent example of such analysis for the all-ferrous state was provided by Chakrabarti et al.[17] Further, the optimized distances are dependent on the precise selection of the DFT functional and the basis set. Below, we refer to the Fe−Fe/Fe−S distances from modeling scenario (i) unless otherwise stated. These representative distances are provided in Table 4; their averaged values are given in Table 3 in comparison to the present EXAFS and earlier XRD determinations.

With regard to the Fe−Fe distances, the DFT structure of the oxidized S = 0 $[4Fe\text{-}4S]^{2+}$ state has six nearly equal 2.68−2.70 Å Fe−Fe distances averaging to 2.69 Å. This is in good agreement with the single distance of 2.72 Å arising from the EXAFS fit (a). Notably, the optimization scenario (iii) without Cα carbons fixations and solvent effects allows for 0.03−0.07 Å expansion in the ferromagnetic mixed-valence $Fe^{2.5+}$−$Fe^{2.5+}$ dimers Fe1−Fe2 (spin-down) and Fe3−Fe4 (spin-up), resulting in a higher 0.07 Å variance within the six Fe−Fe distances.

The DFT structure for the reduced S = 3/2 $[4Fe\text{-}4S]^{1+}$ form has five long 2.68−2.73 Å Fe−Fe distances, and one short distance of 2.62 Å between the two spin-up Fe1 and Fe4 sites. This contraction can be interpreted in terms of valence delocalization in the $Fe^{2.5+}$−$Fe^{2.5+}$ dimer.[40,41] The average Fe−Fe distance of 2.69 Å yet compares well with the EXAFS fit (b)

dx.doi.org/10.1021/ja307027n | J. Am. Chem. Soc. 2013, 135, 2530−2543

Table 4. Representative (Scenario (i)) Optimized Fe−Fe and Bonding Fe−S Distances Derived from the DFT Calculations for the *Av2* [4Fe-4S](SCH$_2$CH$_3$)$_4$ Model[a]

		[4Fe-4S]$^{2+}$ M_S = 0 BS34	[4Fe-4S]$^{1+}$ M_S = 1/2 BS14	[4Fe-4S]$^{0+}$ M_S = 4 BS123
Fe−Fe (Å)[b]	Fe1−Fe2	*2.68*	2.68	**2.56**
	Fe1−Fe3	2.69	2.73	**2.56**
	Fe1−Fe4	2.69	**2.62**	*2.77*
	Fe2−Fe3	2.68	*2.71*	**2.58**
	Fe2−Fe4	2.69	2.71	*2.76*
	Fe3−Fe4	**2.70**	2.69	*2.71*
Fe−S^t (Å)[c]	Fe1−S^t	*2.28*	**2.32**	**2.40**
	Fe2−S^t	*2.26*	*2.29*	**2.41**
	Fe3−S^t	**2.27**	*2.32*	**2.42**
	Fe4−S^t	**2.27**	**2.33**	*2.29*
Fe−S^b (Å)[d]	Fe1			
	−S^{b}2	*2.26*	**2.36**	**2.37**
	−S^{b}3	**2.35**	**2.36**	**2.37**
	−S^{b}4	**2.35**	*2.27*	**2.42**
	Fe2			
	−S^{b}1	*2.24*	**2.35**	**2.37**
	−S^{b}3	**2.34**	*2.31*	**2.38**
	−S^{b}4	**2.35**	**2.34**	**2.37**
	Fe3			
	−S^{b}1	**2.36**	**2.36**	**2.38**
	−S^{b}2	**2.34**	*2.29*	**2.38**
	−S^{b}4	*2.23*	**2.34**	**2.43**
	Fe4			
	−S^{b}1	**2.35**	*2.27*	*2.33*
	−S^{b}2	**2.35**	**2.37**	*2.32*
	−S^{b}3	*2.25*	**2.35**	*2.35*

[a] M_S spin projection and broken-symmetry (BS) states are specified for the three oxidation levels. The Fe site numbering corresponds to the PDB files 2NIP[2] and 1G1M.[3] For comparison of the final EXAFS fits and averaged DFT distances, see Table 3. The distances derived using various optimization scenarios (i)-(iii) are available from Table S4 of the SI. [b] Fe−Fe distances between: **bold** - spin-up sites; *italics* - spin-down sites; normal - opposite spin direction sites. [c] Terminal Fe−S^t distances involving **bold** - spin-up sites and *italics* - spin-down sites. [d] Bridging Fe−S^b; [4Fe-4S]$^{2+/1+}$: **bold** - distances forming the edges of the [4Fe-4S] cubane faces carrying the same-direction spin Fe sites (see the text); *italics* - all other Fe-S^b distances; [4Fe-4S]^0: **bold** - distances to spin-up metal sites and *italics* - the unique spin-down site.

of 2.72 Å, similarly to the [4Fe-4S]$^{2+}$ case. We note that resolution of the reduced state EXAFS data is relatively poor at 0.11 Å, and that a single short Fe−Fe would probably contribute around 5% of the EXAFS intensity. In short, our EXAFS data does not have sufficient *k*-range to resolve this single short interaction, and instead it is reflected in the relatively high structural disorder from EXAFS of 0.067 Å, which compares well to the 0.051 Å calculated using DFT.

In the BS123 model for the S = 4 state of the all-ferrous [4Fe-4S]^0 cluster there are three spin-up Fe^{2+} atoms and one spin-down Fe^{2+}. Each Fe center has 5 majority-spin electrons (which are low in energy and do not participate much in formation of chemical bonds), and one minority-spin electron (which can participate in the formation of weak bonds with neighboring atoms). The minority-spin electrons in the three spin-up irons Fe1, Fe2, and Fe3 can delocalize among themselves, whereas the minority-spin electron on the unique spin-down site Fe4 cannot. This leads the three spin-up irons to have short Fe−Fe distances among themselves averaging to 2.57 Å, and three longer Fe−Fe distances to the unique iron averaging to 2.75 Å. This type of Fe−Fe distance splitting was extensively studied by Chakrabarti et al,[17] based on the XRD structure of carbene-capped S = 4 [4Fe-4S]^0 cluster.[16] The DFT model thus agrees well with fits (d0) and (d3) both providing equal numbers of short and long distances of 2.56 and 2.75 Å, respectively, see Table 2, Table 3 and Figure 6. Notably, the existence of Fe−Fe distances shorter than 2.6 Å is a likely sign of weak but direct iron−iron bonds.[18] The dramatic changes in Fe−Fe distances upon going to the all-ferrous form are therefore evident in both the EXAFS and DFT analysis.

For the Fe−S distances, our DFT calculations on the oxidized [4Fe-4S]$^{2+}$ cluster suggest that sixteen Fe−S distances can be grouped in two sets here: eight long 2.34−2.36 Å Fe−S^b distances averaging to 2.35 Å, and the remaining 2.23−2.28 Å Fe−S^t/Fe−S^b set, averaging to 2.26 Å. Long Fe−S^b distances can probably be rationalized in terms of through-bond ferromagnetic repulsion within two pseudoparallel cubane faces, which span the Fe$^{2.5+}$−Fe$^{2.5+}$ dimers (spin-up face [Fe3, Fe4, S^{b}1, S^{b}2], and spin-down face [Fe1, Fe2, S^{b}3, S^{b}4] as in Figure 6). The overall average for the optimized Fe−S distances is then 2.30 Å compared to 2.29 Å from the EXAFS fit (a). Remarkably, in contrast to the Fe−Fe distances, the Fe−S distances change only marginally between the three geometry optimization scenarios (i−iii) here.

Similarly to the oxidized state, the reduced [4Fe-4S]$^{1+}$ cluster displays a set of eight longer 2.34−2.37 Å Fe−S^b distances. In the BS14 spin state, these longer distances are edges of the two pseudoparallel cubane faces: the [Fe1, Fe4, S^{b}2, S^{b}3] face that spans the spin-up Fe$^{2.5+}$−Fe$^{2.5+}$ dimer and the [Fe2, Fe3, S^{b}1, S^{b}4] face that spans the spin-down Fe^{2+}−Fe^{2+} pair, see Figure 6. The Fe−S^t distances split in two groups, as the metals are found at two oxidation levels now, mixed-valence Fe1 and Fe4 and ferrous Fe2 and Fe3. This splitting is most clearly expressed via optimization scenario (ii), providing the Fe−S^t difference amplitude of 0.05 Å. In summary, the Fe−S distances from DFT are found in the 2.27−2.37 Å range for the reduced cluster, however they can not be easily grouped into sets based on the distance criteria. The average Fe−S distance is 2.33 Å compared to 2.30 Å from the EXAFS fit (b), which is a somewhat worse agreement than for the oxidized level.

For the all-ferrous [4Fe-4S]$^{0+}$ cluster, DFT predicts 2 sets of Fe−S distances. The 4 short 2.29−2.35 Å bonds provided by the unique spin-down metal site (Fe4 in the BS123 spin coupling) average 2.32 Å, and the 12 remaining long 2.37−2.43 Å Fe−S^t/Fe−S^b distances average 2.39 Å. While the 4:12 short-to-long Fe−S distribution matches the 1:3 EXAFS fit (d3) in Table 2, the averaged short/long distances by DFT are 0.11 Å:0.07 Å longer than 2.21 Å:2.32 Å from (d3). The origin of this discrepancy between DFT and EXAFS, significant in comparison to the considered above oxidized and reduced state structures, remains to be understood. We note, however, that the overall averaged 2.37 Å Fe−S distance by DFT compares reasonably with 2.32 Å obtained from another representative fit (d0), as well as from the 1G1M PDB file.

Finally, the overall geometry of [4Fe-4S] clusters can be examined using a spherical coordinate analysis that considers the Fe, S^b, and S^t atoms to lie on approximately concentric circles.[42] This approach, called circumsphere analysis, is detailed in the SI and Table S5. The circumsphere analysis shows that the all-ferrous [4Fe-4S]$^{0+}$ cluster is considerably more distorted away from the ideal of intersecting [4Fe], [4S^b],

dx.doi.org/10.1021/ja307027n | J. Am. Chem. Soc. 2013, 135, 2530−2543

and [4S^t] tetrahedra with a common center, than are the less reduced [4Fe-4S]$^{1+}$ and [4Fe-4S]$^{2+}$ oxidation states.

An important observation from our DFT results is that the *Av2* [4Fe-4S] core interactions are largely governed by the spin-dependent phenomena. The numbers presented in Table S4 (SI) and discussed above confirm that positioning of the cysteine side chains by the protein together with the environment effects, both included in the representative geometry optimization scenario (i), are factors perturbing the broken-symmetry (BS) imposed Fe−Fe/Fe−S interatomic distances distributions. The BS character is most sharply expressed for the all-ferrous state in 3:3 short-to-long Fe−Fe distances sets with ∼0.2 Å gap as confirmed by the present EXAFS, and in line with earlier structure studies.[16,17] Our calculations predict that BS "isomers" in the *Av2* cluster are nearly equienergetic and thus can easily interconvert; therefore, a static mapping between the spin up/down sites and the protein Fe centers (as in Table 4) serves only a modeling purpose. For the all-ferrous cluster, however, Chakrabarti et al. proposed that the protein "locks" the [4Fe-4S] electronic state so that the iron labeled Fe3 in the 1G1M PDB structure is the unique (spin-down) site.[17]

The total charge of the DFT [4Fe-4S](SCH$_2$CH$_3$)$_4$ model is negative and grows in magnitude upon the two reduction steps from −2 to −4 units. This results in noticeably longer upper boundaries of the interatomic Fe−Fe/Fe−S distances for the reduced (net charge of −3) and particularly for the all-ferrous (−4) state due to the electrostatic repulsion. The Fe−S^t distances to the terminal (cysteine) sulfurs were found to be most sensitive to the 2e^- reduction, with their maxima rising by 0.14 Å between the oxidized and all-ferrous states. Notably, the protein effects introduced during the DFT optimization effectively compensate the redox expansion of the model, and ultimately provide a better correspondence between DFT and EXAFS. When the protein effects are omitted in optimization scenarios (ii) and (iii), see Table S4 (SI), again the Fe−S^t bonds in the all-ferrous cluster were found to expand most, by as much as 0.09 Å; in contrast, Fe−S^b distances to the bridging sulfurs are least sensitive to the protein effects. The cumulative expansion of the cluster upon reduction can be characterized in terms of van der Waals (vdW) cavity volume encasing the [4Fe-4S](SCH$_2$CH$_3$)$_4$ model: the ∼550 Å^3 cavity in the oxidized state grows by 2% upon 1e^- reduction, and by 4% upon 2e^- reduction. The surface area of the vdW cavity increases most drastically in the all-ferrous state: ∼504 Å^2 surface in the oxidized state grows by 1% upon 1e^- reduction, and by 5% upon 2e^- reduction. The latter observation is important in view of the largest *Av2* [4Fe-4S] solvent-accessible area known among Fe−S proteins.

In summary, we obtained a very good agreement between the DFT and EXAFS on the Fe−Fe distances of the *Av2* [4Fe-4S] cluster (Table 3); for the oxidized and reduced forms the DFT averages are only 0.03 Å shorter than EXAFS, and for both 3:3 distance groups in the all-ferrous state this deviation is within 0.01 Å only. The match is somewhat less satisfactory for the Fe−S distances. For fits assuming a single Fe−S interaction, the deviation between distances measured by EXAFS and the mean distances calculated by DFT grows as the cluster becomes more reduced, with 0.02, 0.04, and 0.05 Å (d0 in Table 3) overestimation by DFT for the oxidized, reduced, and all-ferrous forms, respectively. Furthermore, our preferred EXAFS fit (d3) in Table 3 for the all-ferrous state comprises 1:3 Fe−S distances; while this is consistent with DFT indicating the equivalent 4:12 ratio, there remains a ∼0.1 Å disagreement on the mean values. It is perhaps relevant that both the bridging and terminal sulfurs are more exposed to the interaction with the protein, while at the same time they screen the Fe sites. The discrepancy in Fe−S distances may thus arise from specific interactions with the *Av2* protein environment, such as hydrogen bonding, missing in the present modeling.

CONCLUSIONS

In this work we have studied the vibrational dynamics and structure of the nitrogenase *Av2* [4Fe-4S] cluster at the oxidized, reduced, and all-ferrous oxidation levels. These data include the first vibrational characterization by any technique for any all-ferrous [4Fe-4S]^0 cluster as well as the first vibrational description of the one-electron-reduced [4Fe-4S]$^{1+}$ form of nitrogenase Fe protein. For the oxidized [4Fe-4S]$^{2+}$ state, analysis of NRVS spectra supported by DFT calculations show that the highest energy modes around 387 cm^{-1} are predominately terminal cysteinate Fe−S^t in their character, while the bridging Fe−S^b modes tend to occur around 379−387, 338, and 274 cm^{-1}. The terminal Fe−S^t modes consistently show higher force constants than the bridging Fe−S^b, in agreement with the greater strength of the Fe−S^t bonding. We observe a systematic 10−30 cm^{-1} stepwise decrease in Fe−S stretching frequencies upon each one-electron reduction. The lower energy bands between 120 and 155 cm^{-1} result from mainly S−Fe−S bending modes, with their localization nearly invariant to the [4Fe-4S] oxidation level. Our empirical force field analyses from NRVS are therefore borne out by parallel DFT calculations, which produce good simulated spectra with PED profiles for Fe−S^t, Fe−S^b, and Fe−Fe that exhibit similar trends.

The EXAFS analysis provides a systematic study of the structural changes in the [4Fe-4S] cluster with oxidation state. The EXAFS interpretation is assisted and constrained by the NRVS data, as the NRVS analysis allows us to derive estimates for the thermal contribution to the disorder of Fe−S and Fe−Fe distances, which in turn allows us to estimate the structural disorder for each observed Fe−S and Fe−Fe interaction. The oxidized [4Fe-4S]$^{2+}$ state showed an essentially symmetric cluster with Fe−S and Fe−Fe distances around 2.32 Å and 2.72 Å, respectively. Addition of one electron produces a modest increase in the spread of Fe−Fe distances, while addition of a second electron to produce the all-ferrous state results in a significant structural change. The structure of the all-ferrous state was resolved using data recorded up to k = 21 Å^{-1} and the simplest model involves equal numbers of two distinct Fe−Fe interactions at 2.56 and 2.75 Å. Importantly, all these EXAFS measurements were performed without a glassing agent like glycerol. A control experiment on the one-electron-reduced [4Fe-4S]$^{1+}$ state using 15% glycerol showed significant conformational change in the cluster.

The [4Fe-4S] cluster distortions for all three oxidation levels were rationalized in terms of spin-dependent phenomena using the broken-symmetry DFT formalism. While including solvation effects improves the correspondence to EXAFS, the calculations indicate that the internal symmetry of the [4Fe-4S] core is essentially invariant to the protein environment. From a set of DFT interpretations, including circumsphere analysis and estimation of the cluster volume and surface, we confirm that the all-ferrous state comprises a highly distorted [4Fe-4S] species. Overall, the DFT calculations and EXAFS results agree very well. The averaged DFT values within the short/long Fe−

Fe interatomic distance sets deviate by at most 0.03 Å from the present EXAFS. For the Fe−S distances in the oxidized and reduced forms, this deviation is within 0.05 Å. For the all-ferrous state, DFT overestimates the best fit 1:3 short/long Fe−S average distances from EXAFS by ∼0.1 Å. An advance in theory might resolve this by including the *Av2* protein environment via a QM/MM scheme instead of the PCM solvation model used here. Application of a somewhat different underlying methodology, such as a functional different from PW91, may also improve the optimized Fe−S bond distances.

Finally, the results highlight the power and symbiotic nature of the combined application of NRVS, EXAFS, and DFT to characterization and understanding of Fe−S clusters in biology. Not only do the three approaches provide complementary information, but the analytical methodologies we have employed are also interdependent. The ability to derive vibrational disorder terms from fits to NRVS spectra substantially assists the analysis and interpretation of EXAFS data. Similarly, the availability of good structural parameters from EXAFS and DFT is an important part of the detailed normal-mode analysis of NRVS spectra. Together, two spectroscopies provide a good framework for calibrating and testing the DFT methodology, and last but not least, the DFT results contribute significant insights to the origins of *Av2* [4Fe-4S] cluster structure and vibrational dynamics revealed by the NRVS and EXAFS experiments.

■ ASSOCIATED CONTENT

Ⓢ Supporting Information

Full experimental and computational methods. Mössbauer spectroscopy results, fits and fitting parameters. Additional details of the NRVS, EXAFS, and DFT analyses. For NRVS: a table of all NRVS-derived Urey−Bradley force-field force constants for *Av2* and model complexes, a table of complete mode assignments with calculated and observed NRVS frequencies, a figure showing full Urey−Bradley force-field simulations for each oxidation state and symmetry model tested, an illustration of the normal mode atomic motion from NRVS analysis, and a figure showing example force field simulations for the all-ferrous $[4Fe\text{-}4S]^0$ state for different structural models. For EXAFS: figures showing deconvolution of the optimum curve-fits for the reduced $[4Fe\text{-}4S]^{1+}$ and all-ferrous $[4Fe\text{-}4S]^0$ states. For DFT: a table of optimized distances from each of the DFT calculation scenarios, and details of the circumsphere analysis for representative DFT structures. This material is available free of charge via the Internet at http://pubs.acs.org.

■ AUTHOR INFORMATION

Corresponding Author

spjcramer@ucdavis.edu; pelmentschikov@mailbox.tu-berlin.de.

Author Contributions

#D.M. and S.J.G. contributed equally to this manuscript.

Notes

The authors declare no competing financial interest.

■ ACKNOWLEDGMENTS

We gratefully acknowledge Prof. Louis Noodleman for insightful discussions. We also thank Drs. Yoshitaka Yoda, Jiyong Zhao, Hongxin Wang, and Eric Dowty for NRVS beamline and theoretical assistance. This work was funded by NIH GM-65440 (S.P.C.), EB-001962 (S.P.C.), GM-39914 (D.A.C.), the DOE Office of Biological and Environmental Research (S.P.C.), the Alexander von Humboldt Foundation (V.P.), the UniCat Cluster of Excellence (V.P.), and the NASA Astrobiology Institute (NAI) Grant NNA08C-N85A (J.W.P.). Use of the APS is supported by the DOE Office of Basic Energy Sciences. Use of SPring-8 beamline BL09XU was with the approval of the Japan Synchrotron Radiation Research Institute (JASRI). Use of SSRL is supported by the DOE Office of Basic Energy Sciences. The SSRL Structural Molecular Biology Program is supported by the DOE, Office of Biological and Environmental Research, and by the NIH.

■ REFERENCES

(1) Burgess, B. K.; Lowe, D. J. *Chem. Rev.* **1996**, *96*, 2983−3011. Howard, J. B.; Rees, D. C. *Proc. Natl. Acad. Sci. U.S.A.* **2006**, *103*, 17088−17093. Peters, J. W.; Szilagyi, R. K. *Curr. Opin. Chem. Biol.* **2006**, *10*, 101−108.

(2) Schlessman, J. L.; Woo, D.; Joshua-Tor, L.; Howard, J. B.; Rees, D. C. *J. Mol. Biol.* **1998**, *280*, 669−685.

(3) Strop, P.; Takahara, P. M.; Chiu, H.-J.; Angove, H. C.; Burgess, B. K.; Rees, D. C. *Biochemistry* **2001**, *40*, 651−656.

(4) Yoo, S. J.; Angove, H. C.; Burgess, B. K.; Hendrich, M. P.; Münck, E. *J. Am. Chem. Soc.* **1999**, *121*, 2534−2545.

(5) Sarma, R.; Mulder, D. W.; Brecht, E.; Szilagyi, R. K.; Seefeldt, L. C.; Tsuruta, H.; Peters, J. W. *Biochemistry* **2007**, *46*, 14058−14066.

(6) Fu, W. G.; Morgan, T. V.; Mortenson, L. E.; Johnson, M. K. *FEBS Lett.* **1991**, *284*, 165−168.

(7) Sen, S.; Igarashi, R.; Smith, A.; Johnson, M. K.; Seefeldt, L. C.; Peters, J. W. *Biochemistry* **2004**, *43*, 1787−1797.

(8) Ryle, M. J.; Lanzilotta, W. N.; Seefeldt, L. C.; Scarrow, R. C.; Jensen, G. M. *J. Biol. Chem.* **1996**, *271*, 1551−1557.

(9) Lindahl, P. A.; Teo, B.-K.; Orme-Johnson, W. H. *Inorg. Chem.* **1987**, *26*, 3912−3916.

(10) Blank, M.; Lee, C.; Hu, Y.; Hodgson, K.; Hedman, B.; Ribbe, M. *Inorg. Chem.* **2011**, *50*, 7123−7128.

(11) Musgrave, K. B.; Angove, H. C.; Burgess, B. K.; Hedman, B.; Hodgson, K. O. *J. Am. Chem. Soc.* **1998**, *120*, 5325−5326.

(12) Hu, Y. L.; Fay, A. W.; Lee, C. C.; Yoshizawa, J.; Ribbe, M. W. *Biochemistry* **2008**, *47*, 3973−3981.

(13) Watt, G. D.; Reddy, K. R. N. *J. Inorg. Biochem.* **1994**, *53*, 281−294. Angove, H. C.; Yoo, S. J.; Burgess, B. K.; Münck, E. *J. Am. Chem. Soc.* **1997**, *119*, 8730−8731. Angove, H. C.; Yoo, S. J.; Münck, E.; Burgess, B. K. *J. Biol. Chem.* **1998**, *273*, 26330−26337.

(14) Seefeldt, L. C.; Hoffman, B. M.; Dean, D. R. *Curr. Opin. Chem. Biol.* **2012**, *16*, 19−25.

(15) Scott, T. A.; Berlinguette, C. P.; Holm, R. H.; Zhou, H. C. *Proc. Natl. Acad. Sci. U.S.A.* **2005**, *102*, 9741−9744.

(16) Deng, L.; Holm, R. H. *J. Am. Chem. Soc.* **2008**, *130*, 9878−9886.

(17) Chakrabarti, M.; Deng, L.; Holm, R. H.; Münck, E.; Bominaar, E. L. *Inorg. Chem.* **2009**, *48*, 2735−2747. Chakrabarti, M.; Münck, E.; Bominaar, E. L. *Inorg. Chem.* **2011**, *50*, 4322−4326.

(18) Torres, R. A.; Lovell, T.; Noodleman, L.; Case, D. A. *J. Am. Chem. Soc.* **2003**, *125*, 1923−1936.

(19) Noodleman, L.; Lovell, T.; Liu, T.; Himo, F.; Torres, R. A. *Curr. Opin. Chem. Biol.* **2002**, *6*, 259−273.

(20) Lindahl, P. A.; Gorelick, N. J.; Münck, E.; Orme-Johnson, W. H. *J. Biol. Chem.* **1987**, *262*, 14945−14963.

(21) Buckel, W.; Hetzel, M.; Kim, J. *Curr. Opin. Chem. Biol.* **2004**, *8*, 462−467. Sarma, R.; Barney, B. M.; Hamilton, T. L.; Jones, A.; Seefeldt, L. C.; Peters, J. W. *Biochemistry* **2008**, *47*, 13004−13015.

(22) Hans, M.; Buckel, W.; Bill, E. *J. Biol. Inorg. Chem.* **2008**, *13*, 563−574.

(23) George, S. J.; Igarashi, R. Y.; Xiao, Y.; Hernandez, J. A.; Demuez, M.; Zhao, D.; Yoda, Y.; Ludden, P. W.; Rubio, L. M.; Cramer, S. P. *J. Am. Chem. Soc.* **2008**, *130*, 5673−5680. George, S. J.; Barney, B. M.; Mitra, D.; Guo, Y.; Igarashi, R. Y.; Dean, D. R.; Cramer, S. P.; Seefeldt, L. *J. Inorg. Biochem.* **2012**, *112*, 85−92.

(24) Xiao, Y.; Koutmos, M.; Case, D. A.; Coucouvanis, D.; Wang, H.; Cramer, S. P. *Dalton Trans.* **2006**, 2192−2201.
(25) Mitra, D.; Pelmenschikov, V.; Guo, Y.; Case, D. A.; Wang, H.; Dong, W.; Tan, M.-L.; Ichiye, T.; Francis, E.; Jenney, J.; Adams, M. W. W.; Yoda, Y.; Zhao, J.; Cramer, S. P. *Biochemistry* **2011**, *50*, 5220−5235.
(26) Spiro, T.; Czernuszewicz, R. S. *Methods Enzymol.* **1995**, *246*, 416−460.
(27) Czernuszewicz, R. S.; Macor, K. A.; Johnson, M. K.; Gewirth, A.; Spiro, T. G. *J. Am. Chem. Soc.* **1987**, *109*, 7178−7187. Backes, G.; Mino, Y.; Loehr, T. M.; Meyer, T. E.; Cusanovich, M. A.; Sweeney, W. V.; Adman, E. T.; Sanders-Loehr, J. *J. Am. Chem. Soc.* **1991**, *113*, 2055−2064. Kern, A.; Nather, C.; Studt, F.; Tuczek, F. *Inorg. Chem.* **2004**, *43*, 5003−5010.
(28) Xiao, Y.; Wang, H.; George, S. J.; Smith, M. C.; Adams, M. W. W.; Francis, E.; Jenney, J.; Sturhahn, W.; Alp, E. E.; Zhao, J.; Yoda, Y.; Dey, A.; Solomon, E. I.; Cramer, S. P. *J. Am. Chem. Soc.* **2005**, *127*, 14596−14606.
(29) Xiao, Y.; Tan, M.-L.; Ichiye, T.; Wang, H.; Guo, Y.; Smith, M. C.; Meyer, J.; Sturhahn, W.; Alp, E. E.; Zhao, J.; Yoda, Y.; Cramer, S. P. *Biochemistry* **2008**, *47*, 6612−6627.
(30) Cotelesage, J. J.; Pushie, M. J.; Grochulski, P.; Pickering, I. J.; George, G. N. *J. Inorg. Biochem.* **2012**, *115*, 127−137.
(31) Poiarkova, A. V.; Rehr, J. J. *Phys. Rev. B* **1999**, *59*, 948−957.
(32) Vila, F. D.; Lindahl, V. E.; Rehr, J. J. *Phys. Rev. B* **2012**, *85*, 024303.
(33) Cyvin, S. J. *Molecular Vibrations and Mean Square Amplitudes*; Elsevier: Amsterdam, 1968.
(34) Fukuyama, K.; Okada, T.; Kakuta, Y.; Takahashi, Y. *J. Mol. Biol.* **2002**, *315*, 1155−1166.
(35) Excoffon, P.; Laugier, J.; Lamotte, B. *Inorg. Chem.* **1991**, *30*, 3075−3081.
(36) Que, L., Jr.; Bobrik, M. A.; Ibers, J. A.; Holm, R. H. *J. Am. Chem. Soc.* **1974**, *96*, 4168−4178.
(37) Dauter, Z.; Wilson, K. S.; Sieker, L. C.; Meyer, J.; Moulis, J. M. *Biochemistry* **1997**, *36*, 16065−16073.
(38) Carney, M. J.; Papaefthymiou, G. C.; Frankel, R. B.; Holm, R. H. *Inorg. Chem.* **1989**, *28*, 1497−1503. Hagen, K. S.; Uddin, M. *Inorg. Chem.* **2008**, *47*, 11807−11815.
(39) Xiao, Y.; Fisher, K.; Smith, M. C.; Newton, W.; Case, D. A.; George, S. J.; Wang, H.; Sturhahn, W.; Alp, E. E.; Zhao, J.; Yoda, Y.; Cramer, S. P. *J. Am. Chem. Soc.* **2006**, *128*, 7608−7612.
(40) Noodleman, L.; Case, D. A. *Adv. Inorg. Chem.* **1992**, *38*, 423−470.
(41) Beinert, H.; Holm, R. H.; Münck, E. *Science* **1997**, *277*, 653−659.
(42) Fee, J. A.; Castagnetto, J. M.; Case, D. A.; Noodleman, L.; Stout, C. D.; Torres, R. A. *J. Biol. Inorg. Chem.* **2003**, *8*, 519−526.